Mechanics of torque generation in the bacterial flagellar motor

Kranthi K. Mandadapu[a,b,1], Jasmine A. Nirody[c,1], Richard M. Berry[d], and George Oster[e,2]

[a]Department of Chemistry, University of California, Berkeley, CA 94720; [b]Chemical Sciences Division, Lawrence Berkeley National Laboratory, Berkeley, CA 94720; [c]Biophysics Graduate Group, University of California, Berkeley, CA 94720; [d]Department of Physics, University of Oxford, Oxford OX1 3PU, United Kingdom; and [e]Department of Molecular and Cellular Biology, University of California, Berkeley, CA 94720

Edited by Howard C. Berg, Harvard University, Cambridge, MA, and approved June 1, 2015 (received for review January 26, 2015)

The bacterial flagellar motor (BFM) is responsible for driving bacterial locomotion and chemotaxis, fundamental processes in pathogenesis and biofilm formation. In the BFM, torque is generated at the interface between transmembrane proteins (stators) and a rotor. It is well established that the passage of ions down a transmembrane gradient through the stator complex provides the energy for torque generation. However, the physics involved in this energy conversion remain poorly understood. Here we propose a mechanically specific model for torque generation in the BFM. In particular, we identify roles for two fundamental forces involved in torque generation: electrostatic and steric. We propose that electrostatic forces serve to position the stator, whereas steric forces comprise the actual "power stroke." Specifically, we propose that ion-induced conformational changes about a proline "hinge" residue in a stator α-helix are directly responsible for generating the power stroke. Our model predictions fit well with recent experiments on a single-stator motor. The proposed model provides a mechanical explanation for several fundamental properties of the flagellar motor, including torque–speed and speed–ion motive force relationships, backstepping, variation in step sizes, and the effects of key mutations in the stator.

bacterial flagellar motor | torque generation | mechanochemistry | molecular motors | steric forces

The bacterial flagellar motor (BFM) is one of only two known protein motors that uses the potential energy stored in the transmembrane ion gradient (the ion motive force, or IMF) instead of ATP, the near-universal cellular energy currency. The other such motor is the F_O motor of ATP synthase, responsible for the synthesis of ATP. Understanding how these ion-driven machines generate useful mechanical work is a fundamental issue in cellular biology.

One of the principle diagnostics for a rotary motor is the relationship between torque and rotational speed. Theoretical models attempt to reproduce these empirically measured relationships. The torque–speed curve of the BFM appears to display two distinct regimes: a constant-torque plateau at low speeds that sharply transitions into a near-linear decrease in torque at high speeds (1). Importantly, recent experiments show that the number of torque-generating units (or stators) is likely not constant across this curve (2). This is akin to a car in which the number of active cylinders changes as the car goes uphill and downhill.

In an attempt to reproduce experimentally measured torque-speed curves, most of the currently published models assume that the number of working stators is constant. However, recent measurements of single-stator torque–speed curves provides insight into the physics of the rotor–stator interaction (3). Here, we focus on the mechanism of torque generation in single-stator motors. Understanding the physics of the torque–speed curve of multiple-stator motors requires consideration of load-dependent stator recruitment, which is beyond the scope of this work.

The recently reported single-stator torque–speed curves (3) make a theoretical reexamination of the BFM's torque generation mechanism especially timely. Currently published models describe torque generation phenomenologically as an energy surface without committing to a specific physical mechanism. Here we combine the currently available structural information with published biophysical and biochemical studies on the dynamical behavior of the motor to propose a mechanically specific and experimentally testable model of torque generation in the BFM.

The BFM consists of a series of concentric rings embedded in the cell envelope connected to an extracellular helical propeller by a flexible hook (Fig. 1). The cytoplasmic C-ring acts as the rotor and the membrane-embedded Mot (Motility protein) complexes act as the stators. A working motor can have between 1 and 11 such stator units. Each stator unit is composed of 4 MotA and 2 MotB helix bundles (4, 5). A MotA bundle consists of four membrane-embedded α-helices linked by two large cytoplasmic loops. Interaction between the cytoplasmic loops and FliG proteins located on the periphery of the rotor is implicated in torque generation. We note that although there is some controversy on the exact number of FliGs, this detail does not affect the main points of our model. For ease of exposition, in the following, we assume that there are 26 FliG "spokes" on the rotor.

The feat of coupling an ion gradient to the generation of mechanical work is attributed to the MotB complexes. These complexes each contain an ion-conducting channel with a negatively charged aspartate residue (Asp32) that binds cations. This residue is one of the most strongly conserved residues across bacterial species (1, 5). The interaction between Asp32 and a cation passing through the inner bacterial membrane (between the periplasm and the cytoplasm) was previously suggested to induce conformational changes in the stator complex, resulting in the torque-generating power stroke (5).

Significance

Locomotion in many bacterial species is driven by the rotation of one or more long flagellar filaments, each powered by a bacterial flagellar motor (BFM) at its base. The BFM, then, plays a central role in processes such as chemotaxis, bacterial pathogenicity, and biofilm formation. Using information from structural and biophysical experiments on the BFM, we construct a testable model for the mechanism of torque generation. Our model is, to our knowledge, the first to propose and test a specific physical mechanism for this process, and it provides a mechanical explanation for several fundamental properties of the BFM. In addition to fitting current experimental results, model predictions suggest further experiments to shed light on various aspects of motor function.

Author contributions: K.K.M., J.A.N., and G.O. designed research; K.K.M., J.A.N., and G.O. performed research; and K.K.M., J.A.N., R.M.B., and G.O. wrote the paper.

The authors declare no conflict of interest.

This article is a PNAS Direct Submission.

[1]K.K.M. and J.A.N. contributed equally to this work.

[2]To whom correspondence should be addressed. Email: goster@berkeley.edu.

This article contains supporting information online at www.pnas.org/lookup/suppl/doi:10.1073/pnas.1501734112/-/DCSupplemental.

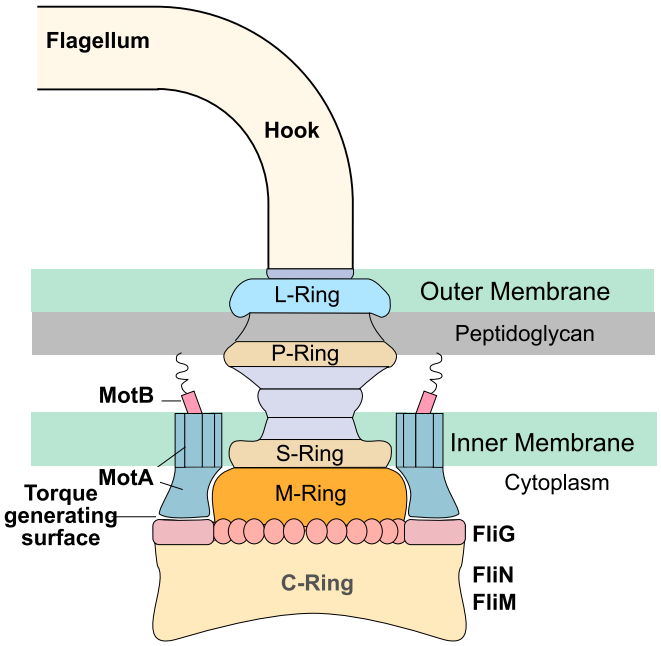

Fig. 1. Schematic showing the basic parts of the BFM. A bacterium has, on average, four flagellae, each attached to the basal body of a motor via a flexible hook. The M, S, and C rings of the basal body are together called the rotor. FliG proteins (26 copies of which are assumed here) are placed around the periphery of the C ring. These interact with the MotA loops of the stator to generate torque and rotate the flagella. Stators are composed of MotA and MotB subunits, the latter of which attaches the stators to the peptidoglycan layer, allowing for torque generation via the MotA–FliG interaction. A motor can have between 1 and 11 engaged stators, depending on the load (2, 31, 32).

A crystal structure of the stator complex will be necessary for a complete understanding of the power stroke. However, the available structural knowledge, combined with information about the motor's dynamical performance, is sufficient to propose a plausible model that is experimentally testable. Using this information, we present a mechanical model for torque generation involving proline-induced conformational changes in MotA cytoplasmic loops (5, 6). To the best of our knowledge, our model is the first to incorporate known structural information about the BFM stator and rotor complexes into a quantitative physical mechanism for the generation of the power stroke. As part of this study, we aim to address the following fundamental questions: (*i*) What are the kinematics and dynamics of the BFM power stroke? (*ii*) What role do charged residues on the stator and rotor play in torque generation, and how does this role explain mutational experiments which show only a partial reduction in motor efficiency? (*iii*) What is the physics behind the shape of the torque-speed curve for single-stator motors? (*iv*) Why does the motor exhibit backsteps even in the absence of an external 'reversal' signal (usually the small protein CheY-P)?

In addressing these issues, we primarily discuss the proton (H^+) powered motor of *Escherichia coli*. However, our model is sufficiently general so as to apply to the sodium (Na^+) powered motors found in alkalophiles and marine *Vibrio* species.

Mechanochemical Model

An Electrosteric Power Stroke. Due to the modest magnitude of the forces involved relative to thermal fluctuations, it has long been assumed that nearly any form of interaction between rotor and stator is sufficient to explain the rotation of the BFM (1). For this reason, previous models have avoided committing to a particular physical origin for these forces, instead treating the interaction between the stators and the rotor phenomenologically as a free-energy surface and the stator as an ad hoc stochastic stepper (7–9).

However, knowledge gained from recent structural (4, 10, 11) and biophysical (3) studies has led us to conclude that the power stroke of the BFM is electrosteric—that is, it is driven by both electrostatic and steric forces. Hence, we propose a mechanochemical model consisting of two phases. (*i*) Before the power stroke, electrostatic forces position the stator. (*ii*) Once positioned, the stator delivers a steric push (i.e., a contact force) on a FliG protein located along the periphery of the rotor. A more detailed description of the nature of contact forces is found in *SI Text* and in ref. 12.

In the following, we lay out the assumptions involved in the construction of our model, followed by a detailed description of the mechanism. Details of the mathematical formulation are provided in *Materials and Methods* and *SI Text*.

Electrostatic Forces Steer the Stator into Place. The first step in constructing our model is the steering and positioning of the stator by electrostatic forces. This hypothesis originates from the results of the mutagenesis experiments performed by Zhou et al. (13). These studies were aimed at elucidating the structure of the MotA loops. They found that mutations of certain charged residues on the cytoplasmic portions of the loops degraded—but did not eliminate—motor function. Notably, the deleterious effects of mutations on the stator were often countered by corresponding mutations (in particular, compensating charge reversals on the FliGs). Certain mutations were also found to have very small effects, or even to cause slight improvements, on bacterial motility.

These results correspond to the idea that mutations of charged residues may result in imperfect steering and consequently in a less efficient—but still functioning—power stroke. Similarly, certain mutations may position the cytoplasmic loops closer to the adjacent FliG, resulting in a larger power stroke and corresponding improved motility.

Because detailed structural information on the stator is not yet available, we performed a simple example calculation to demonstrate how electrostatic interactions can position the stator ready for a power stroke. Explicit calculations, as well as a full explanation of model assumptions, can be found in *SI Text*. For computational convenience, we approximate the important charged residues on the FliG (Flagellar motor switch protein G) proteins (10) and stator loops (14) implicated in torque generation. The assumption that FliG proteins can be modeled as dipoles is based on previous studies (10, 15). Modeling the electrostatic forces between the stator and rotor by point charge interactions produces results comparable to those obtained from a dipole approximation.

The distribution of observed rotor step-sizes has been shown experimentally to be centered around $2\pi/26$ radians (~13.8°), the average spacing between consecutive FliGs (16, 17). The positioned charges result in a weak electrostatic force that is sufficient to position the MotA loop without significantly wasting energy to free the stator at the end of the power stroke. Furthermore, the width of the well leads to somewhat imprecise positioning. Although this result is hardly unexpected, the wide spread of this distribution—in particular, the tendency toward smaller step sizes—has been somewhat puzzling.

Because a wide energy well may result in stators being positioned at nonoptimal locations, electrostatic positioning may contribute to this variance. Because we propose that the stator's power stroke is imparted via a contact force on the rotor, imperfect electrostatic positioning will result in the stator being in contact for only a portion of its trajectory. This results in the stator delivering a stroke that is smaller than average. Of course, imperfect steering is not likely to be the only factor determining the variance in the observed step size distribution: The uneven spacing of FliGs along the periphery of the rotor (18, 19), as well as experimental errors, is also likely to contribute.

Note that, in the case of a reciprocal motion of the stator, attractive electrostatic forces strong enough to comprise the entire

power stroke would require a nonnegligible energy to separate the stator and the rotor at the end of the power stroke. This penalty for letting go would likely obviate the rotor torque, resulting in a motor with a far lower Stokes efficiency (20) than has been calculated for the BFM (~95%) (1). In contrast, the mechanism we propose here efficiently generates mechanical work from the ion motive force.

We note that the above calculation is speculative: Changes in parameter choices will vary the resulting energy landscape. However, our mechanism presupposes that the energy well produced by the electrostatic interactions will be shallow and wide (Fig. 2). We have performed an example calculation to show that such a mechanism is feasible given our limited structural information. A more precise calculation can be performed only when more detailed structures are available.

Motion About a Proline Hinge Provides a Steric Push. As proposed previously (5), we assume that the steric portion of the power stroke is the result of a conformational change in the cytoplasmic MotA loop. Evidence of such conformational changes has also been shown experimentally (21). In our model, this motion consists of hinged movements of the MotA helices that result in a "kink and swivel" motion, as shown in Fig. 3 (6). The steric mechanism proposed below remains valid regardless of which residue, or group of residues, on the MotA/MotB helices acts as the inducer. However, we have chosen to focus on MotA's Pro173 residue because (*i*) along with Asp32 on MotB, this amino acid is strongly conserved across bacterial species (22) and (*ii*) previous molecular dynamics simulations have found that proline residues induce hinges in transmembrane helices (6), resulting in a movement analogous to the one proposed in the model. The specific mechanism we propose is as follows.

When a cation binds to the negatively charged Asp32 residue on MotB, the hydrogen bonds (including those of water) in the vicinity of Asp32 and Pro173 on the A3 helix of MotA collectively rearrange. This rearrangement induces an elastic strain in the MotA–MotB complex centered around the proline residue in the A3 loop of MotA. Fig. 3*A* shows a candidate scenario, where the carbonyl group of residue 169 on MotA forms a hydrogen bond with Asp32 on MotB after proton binding, as proposed in ref. 5. This elastic strain induces the kink and swivel movement around the proline residue and drives the proposed motion of the lower part of the A3 helix, constituting the power stroke (see Fig. 3*B*). The binding of the ion and the rearrangement of the hydrogen bonds (10^{-12} s to 10^{-9} s) are near-instantaneous processes compared with the much slower motion of the kink and swivel conformational change (10^{-5} s to 10^{-3} s). Thus, the chemical steps can be treated as transitions between states in a Markov chain.

The above proposal is supported by a few simple calculations. The maximum torque of the BFM in *E. coli* is ~2,000 pN·nm (23). Given that up to 11 torque-generating units may be acting, this corresponds to a maximum motor torque of ~200 pN·nm per stator (24). As the radius of the motor is ~20 nm, the force generated by a single stator during a power stroke is ~10 pN. Direct observation of stepping behavior has shown that the motor takes 26 elementary steps per revolution, corresponding to a displacement of ~5 nm per step. As explained below, our model supposes that each elementary step is actually composed of two half-steps, each imparted by the power stroke of a MotA helix. This results in a displacement of ~2.5 nm per power stroke. Molecular dynamics studies show the angles subtended by proline hinge motifs from various transmembrane helices to be between 18° and 25° (6). From this, we can estimate the length of the cytoplasmic loop measured from the proline hinge to its tip to be ~ 7 nm, a reasonable estimate as the majority of the stator residues have been shown to extend into the cytoplasm (13). Such a lever arm would result in ~25 pN·nm (~ 6–8 k_BT) of work per half-step, corresponding to the rearrangement of one to two hydrogen bonds (and the free energy released by the passage of one proton). This energy barrier is sufficient to ensure an efficient directional process, as suggested in ref. 25.

An In-Phase Two-Cylinder Engine. There are four MotA subunits in each stator complex; see Fig. 4 for a schematic of the stator structure. Our model supposes that two of these subunits are inactive during torque generation while the motor is moving predominantly in a single direction. We base this presumption on the idea that switches between counterclockwise (CCW) and clockwise (CW) rotation result from changes in FliG orientation

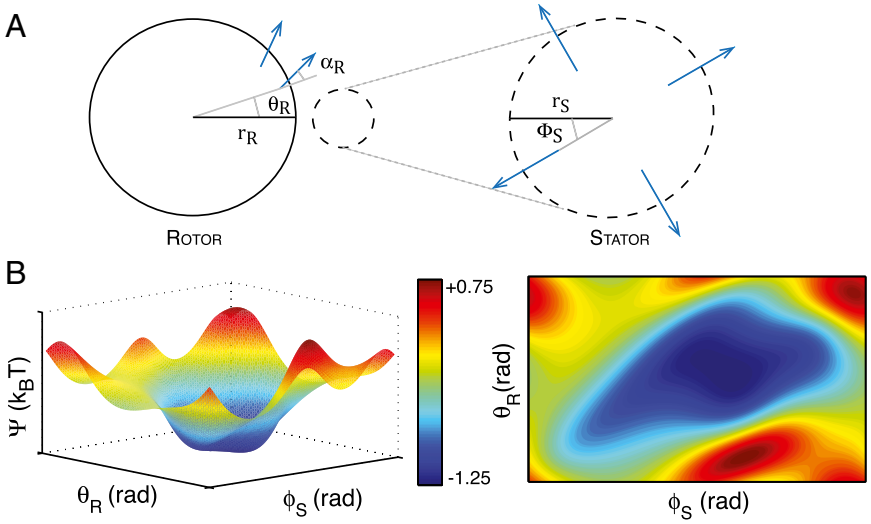

Fig. 2. The predicted energy landscape during electrostatic steering. (*A*) Schematic of rotor and stator configurations; ϕ_S and θ_R are the angular coordinates of the stator and the rotor with respect to the horizontal; α_R is the positive angle of the individual FliGs with respect to the radius. Blue arrows denote the direction of the dipole (10, 15). (*B*) Predicted surface and contour plots of the electrostatic energy vs. the stator and rotor angles. The predicted surface shows the existence of a wide and gently sloping energy well. Note that ϕ_S and θ_R are periodic variables with periods $\pi/2$ and $\pi/13$, respectively; the above plots show one period of each. Our calculations consider a single stator centered at (21,−2,1) with the rotor centered at the origin (all distances in nanometers). Computations using this dipole approximation suggest a well of depth ~1 k_BT for this configuration (see *SI Text* for details).

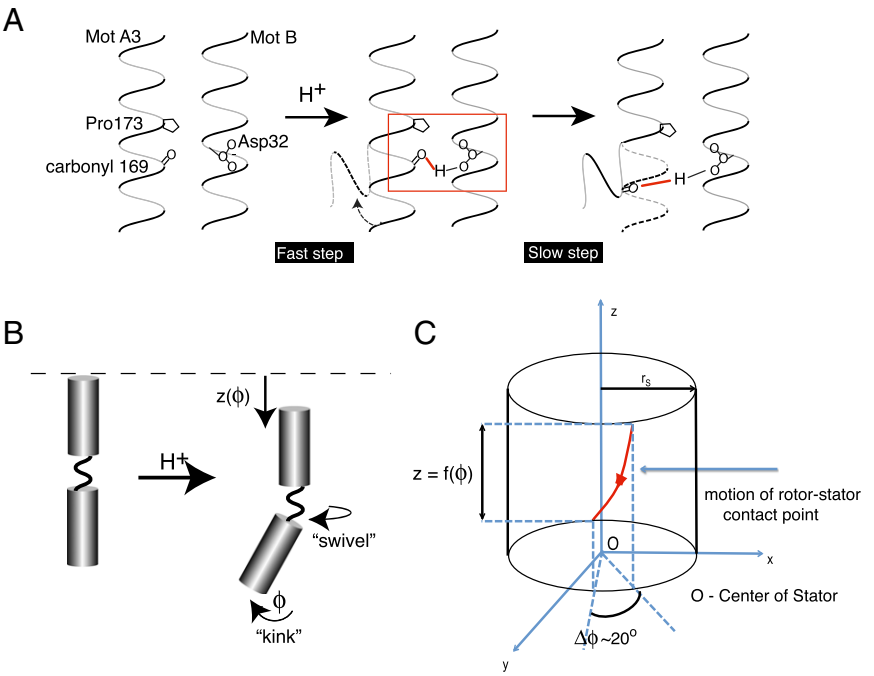

Fig. 3. Ion binding onto Asp32 induces a kink and swivel conformational change (6). (*A*) Binding of a proton to Asp32 of MotB drives a rapid local reorganization of hydrogen bonds (including those of water). In particular, we focus on the creation of a hydrogen bond between the side chain of MotB's Asp32 and the carbonyl group of MotA's residue 169. Ion binding thus creates a local elastic strain in the MotA helix. The release of this strain leads to the proposed conformational change in MotA about the Pro173 residue. Adapted from Kim et al. (5). (*B*) Upon ion binding, MotA undergoes a rapid conformational change consisting of three motions: (*i*) a bending about Pro173 ϕ, (*ii*) a downward motion, $z(\phi)$, and (*iii*) a rotation about its central axis. Inspired by the work of Cordes et al. (6), we propose that this kink and swivel motion generates the power stroke. Importantly, we note that this figure is a 2D depiction of a 3D process, with the motion of the loop extending out of the plane of the page. (*C*) Our envisioned motion of the contact point between a FliG and a stator loop during the power stroke. The kink and swivel motion induces the contact point to follow a helical path on a cylinder of radius approximately equal to the radius of the stator. For simplicity, we assume that the vertical motion is a function of the angle ϕ subtended by the stator loop. Therefore, we explicitly model only the rotational motion ϕ of the stator loop.

(15). Given this, we propose that two MotA loops are responsible for the power stroke in one direction, whereas the other two interact with the alternately oriented FliG to drive rotation in the other direction. We suppose that loops 1 and 3 are responsible for CCW motion and loops 2 and 4 are responsible for CW motion, but note that this designation is arbitrary. This mechanism predicts that the intrinsic mechanics for power strokes in both directions are equivalent; this has been observed experimentally (17).

We propose that an elementary step is composed of a pair of power strokes, analogous to the mechanism of a two-cylinder engine. Experiments on motors driven at extremely low speeds may allow the direct observation of these substeps, in support of our model. This can be done using chimeric sodium-driven flagellar motors. As extremes in sodium concentration are tolerated far more easily than extremes in pH, these chimeric motors can be driven at very low sodium motive forces (SMFs). Thus far, speeds as low as 10 Hz have been obtained (16).

A two-ion mechanism can either be in phase, in which the energetic profiles of the two stator loops are identical, or out-of-phase, in which their dynamics are offset by a half-cycle. In an experiment using a slowly driven chimeric motor, measuring the rate-limiting step between mechanical substeps can differentiate between these two scenarios. For example, if slower ion binding (e.g., by lowering IMF) extends the dwell time between half-steps, the out-of-phase engine model is supported.

The mechanics of these two scenarios are equivalent within the framework of our model. For this reason, we discuss only one of these mechanisms in detail: the one in which the two stator loops act in phase with each other (as shown in Fig. 5*B*). We choose this alternative because the passage of two protons across a membrane provides more energy, which contributes (along with the work done by the MotA loops) to a more reliably directional process in the presence of thermal noise. Interestingly, a single proton passage under standard conditions generates $\sim$ 6 k_BT, slightly less than the calculated length of "time's arrow" (the energy barrier required for a such a reliably directional process) (25).

Full Revolution Requires the Passing of at Least 52 Protons

Our model for torque generation assumes that the rotation of the BFM is tightly coupled to the transmembrane ion gradient. This means that each elementary power stroke is tied directly to the passage of protons across the membrane. Given our prior assumption of 26 elementary steps per revolution, our model thus requires 52 protons for a full revolution. Previously, a lower bound for the number of ions per full revolution was determined by calculating the work done as $\langle\tau\rangle \times 2\pi$ and equating it to the free-energy $n\times$ IMF, where n is the number of ions per revolution and IMF is the ion motive force, as before (3). The above calculation resulted in an estimate of $n = 37$, lower than the 52 ions per revolution supposed by our model.

This discrepancy can be explained as follows. Although the above is indeed a lower bound, a tighter bound can be computed. The calculation of work as stated above suggests that the power output per revolution is $\bar{P} = \langle\tau\rangle\langle\omega\rangle$. However, power is formally calculated as $P = \langle\tau\cdot\omega\rangle$, which differs from $\bar{P}$ by a covariance term, $\mathrm{cov}(\tau,\omega)$. This follows from the fact that, for any two stochastic processes X and Y, $\langle XY\rangle = \langle X\rangle\langle Y\rangle + \mathrm{cov}(X,Y)$.

Note that the number of protons per revolution assumed by our model is also a lower bound; that is, we have assumed that 52 working ions are required per revolution. Many factors can result in the passing of more ions than predicted, including leakiness of

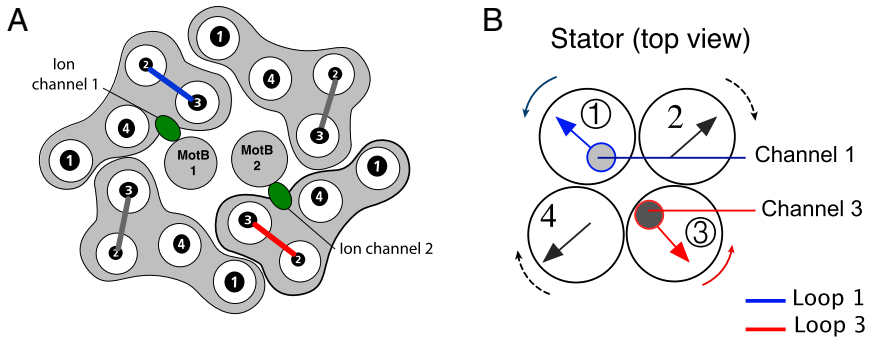

Fig. 4. Stator structure and coordinated motion between stator subunits. (*A*) Proposed arrangement of stator components as viewed from the periplasm. A stator has four MotA helix bundles, each consisting of four α-helices. The four MotA subunits surround a pair of MotB helices. The ion channels associated with the MotBs (shown in green) contain the Asp32 residues essential for proton binding. The stator is attached to the peptidoglycan via a linker region on MotB. The power stroke is delivered to the rotor FliGs by the cytoplasmic loops between helices A2 and A3 in each MotA bundle (shown as solid bars). Loops 1 and 3 (highlighted in blue and red, respectively) are associated with the ion channels. Adapted from Braun et al. and Kim et al. (4, 5). (*B*) Due to the helical structure of the MotA loops, we can make an analogy between their motion and that of a bundle of four gears. Our model proposes that loops 1 and 3 (shown in blue and red, respectively) drive CCW rotation via contact with FliG, whereas loops 2 and 4 drive CW rotation.

the ion channels, loose coupling between the rotational and vertical movements of the stator, irregular arrangement of FliGs around the rotor, or imperfect placement of stators by electrostatic steering forces. This can be quite easily extended within our mathematical framework by replacing the step function associated with ion binding with a sigmoidal function.

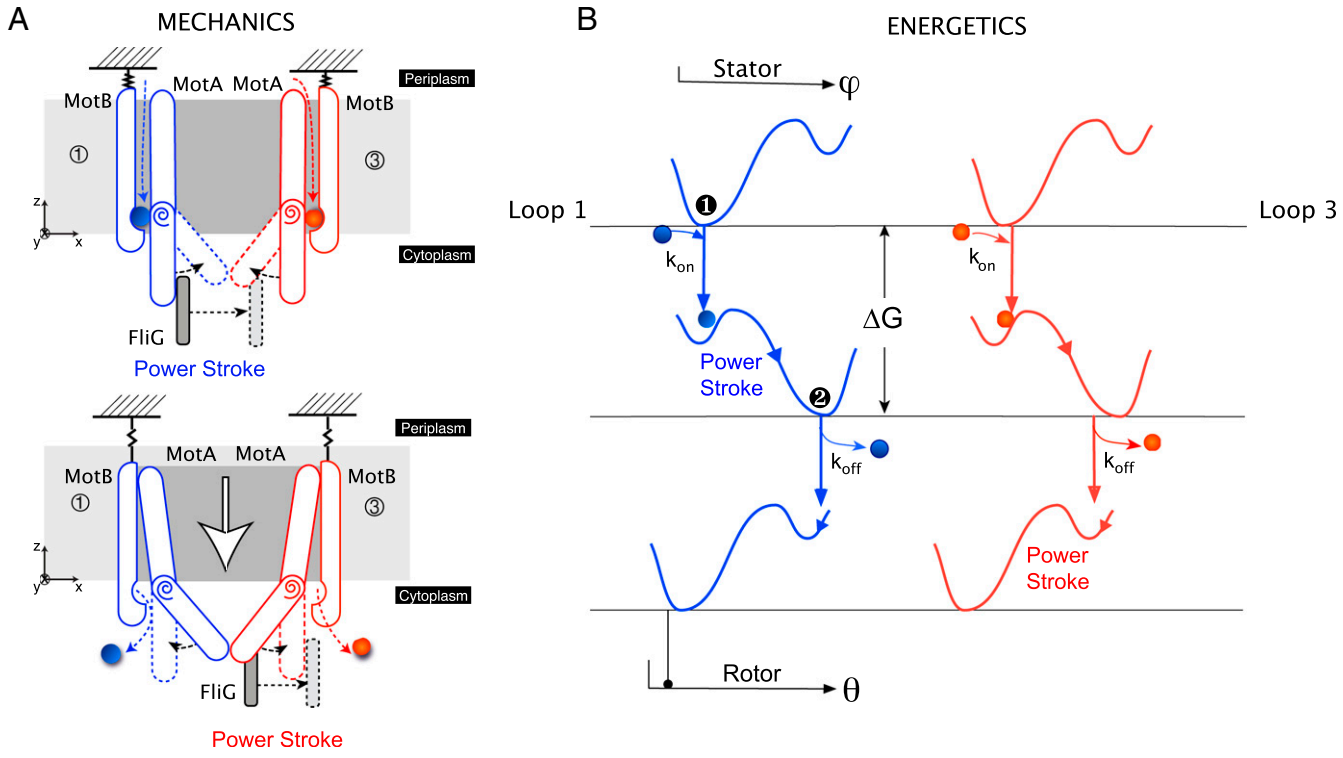

Fig. 5. Dynamics of the rotor–stator interaction. (*A*) Mechanics of the power stroke. (*Top*) After the initial electrostatic steering, two protons bind to the charged Asp32 residues on the MotBs. The consequent rearrangement of hydrogen bonds induces an elastic strain in the straight MotA loops. Release of this strain results in synchronous kink and swivel motions about the proline hinge in both MotAs. As a result, a steric push is imposed on FliG, and the first half of the power stroke is performed by loop 1. Importantly, this motion also has a vertical component—the loops lower themselves out of the membrane. (*Bottom*) The lowering of the MotA loops exposes the protons in MotB to the cytoplasm, whereupon they are released. This results in a reset of the MotA loops, during which loop 3 carries out the second half of the power stroke. We note that this image depicts a 2D projection of a 3D motion: The motion of the stators is not constrained to the plane of the page. An observer sitting on the rotor axis sees the stator inchworm walking along the rotor using the FliGs as steppingstones. (*B*) Energetics of the power stroke. Because the two loops move in phase with each other, their energetic pictures are identical. We describe the free-energy landscapes using double-well Landau potentials. These landscapes are shown in blue for loop 1 and red for loop 3 with respect to the angles of the stator ϕ and rotor θ. We model the stator and rotor interaction using a steric force. This ensures that their motion and the values of the corresponding angles are very tightly tied to one another. The initial entrance of the proton into the ion channel (k_{on}) places the system within k_BT of the energy barrier. Thermal motions then result in the first half of the power stroke (*Top* and *Middle*). Exit of the protons into the cytoplasm (k_{off}) drives the reset, and the second half of the power stroke (*Middle* and *Bottom*).

The Mechanical Escapement. Fig. 5*A* depicts the mechanics associated with the power stroke. We choose the angle subtended by a stator loop ϕ_S^i with respect to the bilayer normal (where i corresponds to the loop number) as the order parameter. That is, we consider the energy landscape along the arc length of the mechanical trajectory of the stator loop. A stator loop has two stable configurations: straight ($\phi_S^i = 0°$) and bent ($\phi_S^i \sim 20°$). Both of these configurations correspond to energy minima in different chemical environments: When the negative Asp32 is not neutralized by a proton, the loops prefer to maintain a straight posture ($\phi_S^i = 0°$). The presence of bound protons induces a free-energy change sufficient such that a thermal fluctuation can induce the conformational change to the bent state ($\phi_S^i \sim 20°$).

During a power stroke, the entire stator complex undergoes a collective gear-like motion as shown in Fig. 4*B*. The conformational change due to the hopping on of the ion produces the first half of the power stroke: Here, loop 1 pushes the FliG, while loop 3 is put in place to carry out the second half of the power stroke during the reset (Fig. 5*A*). This reset corresponds to the hopping off of the proton, resulting once again in the stator loops surmounting the energy barrier between configurations and reverting to the straight position ($\phi_S^i = 0°$). Note that the numbering of the loops is arbitrary; the mechanism proposed here is equivalent to one in which loop 1 performs the first half of the power stroke and loop 3 performs the second.

In summary, a torque generation cycle by a single stator of the BFM proceeds as follows:

i) Electrostatic interactions between charged residues on MotA and FliG steer a stator tip close to a rotor FliG.

ii) In the presence of a membrane potential, the two MotB aqueous ion channels open and two protons bind to the negatively charged Asp32 residues on the MotBs. This triggers a reorganization of the hydrogen bonds in the vicinity of the Pro173 on MotA (see Fig. 3*A*).

iii) The hydrogen bond rearrangements induce elastic strain in the straight MotA loops. This strain drives a kink and swivel motion of the MotA loop, increasing the bend angle (from $\phi_S^i = 0°$ to 20°, as shown in Fig. 3*B*).

iv) One MotA loop (loop 1, shown in blue in Fig. 5*A*) applies a steric push to the nearest FliG, resulting in one half of a power stroke.

v) At the same time, the movement of the stator ion-binding pocket moves downward so that the pocket is exposed to the cytoplasm. The ion channel is now closed to the periplasm. The protons hop off MotB into the cytoplasm, now inverting the strain in the bent MotA loops.

vi) The inverse strain drives the movement of the loops in the reverse direction, straightening the bent MotAs (i.e., from $\phi_S^i \sim 20°$ to 0°).

vii) The other MotA loop (loop 3, shown in red in Fig. 5*A*) now applies a steric push to the same FliG, completing the second half of the power stroke.

Consequently, to the rotor, the stator appears to be an "inchworm" stepper with FliGs as the stepping stones.

Results and Predictions

Using the mathematical model described in *Materials and Methods*, we performed both analytic calculations and numeric stochastic simulations. Statistics from simulated trajectories—an example of which is shown in Fig. 6*A*—were used to calculate various experimental quantities including average motor torque and angular speed.

In the sample trajectory for the rotor motion, the duration of a power stroke (T_m) and the waiting time between consecutive power strokes (T_w) are highlighted in orange and purple, respectively. The highlighted power stroke shows two half-steps, corresponding to the two sequential steric pushes by the two MotA loops involved. As in experimental trajectories, occasional reverse steps are also observed in our simulations, one of which

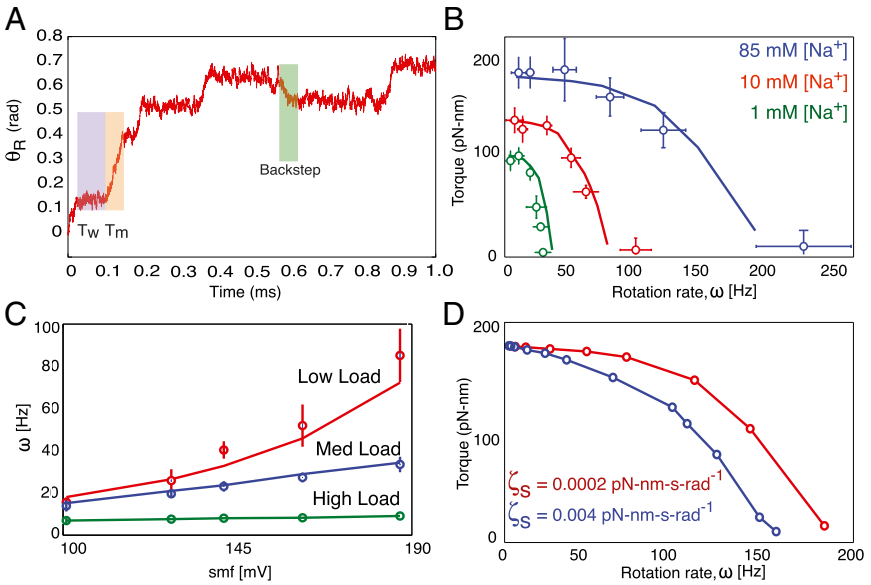

Fig. 6. Summary of recent experiments and comparisons with model simulations. Results are derived from numerical simulations. In all plots, model calculations are shown by solid lines, and experimental data are shown as open colored circles. (*A*) Sample trajectory generated by the model. Moving (T_M) and waiting (T_W) times are shown with orange and purple backgrounds, respectively. Two half-steps separated by a very short pause can be seen in the highlighted forward step (orange). Occasionally, reversals (shown with green background) appear when MotA loops 2 and 4 are engaged due to conformational changes in FliG. (*B*) Single-stator torque–speed curves measured in a chimeric sodium motor for various sodium concentrations at pH 7.0. Curves show a concave-down shape, with the length of their plateaus being SMF dependent [data from Lo et al. (3)]. (*C*) Motor speed vs. SMF in a chimeric sodium motor shows a nearly linear relationship across various loads [data from Lo et al. (3)]. (*D*) Effect of stator viscosity on the shape of BFM torque–speed curves. The reduction in the plateau region is mainly due to the nature of the steric forces during the power stroke.

Table 1. List of parameters with units, values, and reference

Parameter	Definition	Units	Values	Reference
R	radius of the rotor	nm	20	(1)
r_S	radius of the stator	nm	2	—
ℓ_P	length of the proline hinge arm	nm	7	(13)
ζ_S	drag coefficient of the stator	pN·nm·s·rad^{-1}	0.0002	—
ζ_R	drag coefficient of the rotor	pN·nm·s·rad^{-1}	0.017	—
ζ_L	drag coefficient of the load	pN·nm·s·rad^{-1}	0.0–10	(33)
ϕ_S	angular position of the stator	rad	—	—
θ_R	angular position of the rotor	rad	—	—
θ_L	angular position of the load	rad	—	—
κ	hook spring constant	pN·nm·rad^{-1}	1,000	(34)
N	number of stators	—	1–11	(33)
τ	rotor torque from stator	pN·nm	—	—
f_n	white noise	—	—	—
Ψ	electrostatic potential	—	1.5–2 k_BT	—

is shown in the sample path in Fig. 6*A*. An explanation for backsteps that is compatible with our model is provided below.

The results shown in Fig. 6 were obtained via simulation. Analytic calculations on an approximate deterministic model (explicitly provided in *SI Text*) were also performed for illustrating different aspects of the model. These calculations were also used to obtain suitable ranges for the parameters (e.g., stator and rotor drags) used in Langevin simulations.

Single-Stator Motors Exhibit Concave-Down Torque–Speed Curves. Until recently, BFM experiments were performed on motors with multiple stators, with no direct accounting for the number of engaged stators at a given load. Therefore, the existence of the torque–speed plateau and "knee" have been assumed to be innate characteristics of the rotor–stator interaction, largely because there was no evidence to the contrary. However, Lo et al. (3) performed experiments using a chimeric single-stator motor showing smoother torque-speed curves without a dramatic plateau as observed for wild-type motors. Although these curves are still concave-down in shape, the extents of the plateau regions are quite variable and depend on the IMF.

The physics behind the two regimes of the torque–speed curve have been interpreted by previous models as a competition between waiting and moving timescales (7, 8). Thus, the general concave-down shape is largely independent of the exact structural and mechanistic details of the model. It requires only that the model is tightly coupled and the moving time exceeds the waiting time at high loads. Our model for single-stator motors fulfills both of these properties.

Our simulations show torque-speed relationships consistent with these single-stator experiments (Fig. 6*B*). The behavior of the torque–speed curves results from a competition between the time taken for a mechanical half-step (T_M) and the waiting time between ion-binding events (T_W). For example, our simulations show that the average time in moving a half-step $\langle T_M \rangle$ can be ∼20 ms at high loads and ∼0.01 ms at low loads. The average waiting time under standard conditions $\langle T_W \rangle$ is ∼0.2 ms (8). Therefore, at low loads, the motor is in a kinetically limited regime, where the waiting time between steps is generally higher than the time required to complete a step. Conversely, the motor is mechanically limited at high loads when $\langle T_M \rangle > \langle T_W \rangle$, resulting in the observed plateau. Consequently, as shown in Fig. 6*B*, this plateau region grows smaller as the IMF decreases (i.e., as $\langle T_W \rangle$ increases).

This competition is also manifested in the relationship between speed and IMF: Speed depends linearly on IMF at high loads, but in a slightly nonlinear fashion at low loads (Fig. 6*C*). Given that the rotor moves $2\pi/26$ radians per step, the speed of the rotor (ω_R) can be approximated as

$$\omega_R \approx \frac{2\pi}{26} \times \frac{1}{\langle T_M \rangle + \langle T_W \rangle}.$$

At high loads, $\langle T_M \rangle \gg \langle T_W \rangle$. Because the time to complete a power stroke is inversely proportional to the ion motive force, $\langle \omega_R \rangle \propto$ IMF at high loads. In contrast, the waiting time eclipses the time for a mechanical step at low loads, and therefore $\omega_R \propto 1/\langle T_W \rangle \propto \exp(q \times \mathrm{IMF}/k_BT)$. Further details to this end are provided in *SI Text*.

Backstepping in the Absence of CheY-P Is Due to Thermal Flipping of FliG. The BFM plays a central role in bacterial chemotaxis: The direction of rotation of the motor determines whether a bacterium will move in a straight line (CCW) or "tumble" (CW) to move in a random new direction. This switching is typically initiated via a signal transduction pathway, in which a response regulator protein, CheY, is phosphorylated into an activated form, CheY-P, to induce tumbling. For more information on this pathway and bacterial chemotaxis, we refer the reader to several excellent reviews (26, 27).

However, occasional backsteps (e.g., CW motion during primarily CCW rotation) are observed even in the absence of CheY-P. This has been attributed to microscopic reversibility, of which three possible models are discussed in *SI Text*. For example, Mora et al. ascribed switching in the BFM to the diffusive motion of the rotor through a "bumpy" 26-fold periodic potential (28). However, recent structural studies have found that there exist two main configurations for the FliGs (15, 17), lending support to the idea that a flipping between these states is the molecular basis for backstepping. We note that despite a general agreement on the existence of two distinct FliG configurations, the exact nature of the conformational change to the CCW direction remains controversial.

In our model, the probability of observing a backward step is equivalent to the probability of finding a FliG oriented in the CW state (assuming a primarily CCW-rotating motor). Within the framework of our model, whenever a FliG changes its state and is close to a stator, then the stator uses loops 2 and 4 to apply a contact force and pushes the FliG in the CW direction. To model the flipping between CW and CCW states for the FliGs, we use a nearest-neighbor periodic Ising model with the 26 FliGs arranged on a one-dimensional ring. Such models have been used successfully to explain rotational switching (see, e.g., refs. 29 and 30).

In our model, when the FliGs are oriented at an angle of roughly 10–20° with respect to the radial direction, as shown in

Fig. 2*A*, the motor moves in the CW direction by virtue of contact forces from loops 2 and 4. Conversely, when the FliGs are pointed either orthogonal or at an angle of 180° with respect to the CW orientation, the motor steps in the CCW direction using loops 1 and 3. The numerical values for the above parameters will likely change with the resolution of a structure. However, the above calculation is meant to demonstrate the general framework of our predicted mechanism, which is independent of these choices. Using an Ising model for the flipping of FliGs, we calculate the probability of a backstep to be ∼8%. This probability was calculated to be ∼7.3% from stepping statistics collected by Sowa et al. (16), demonstrating that a backstep might indeed be simply due to fluctuations in FliG orientation. Further details on these calculations are provided in *SI Text*.

High Stator Drag Reduces the Torque–Speed Plateau Region. Because our mechanism crucially depends on steric forces, we expect the drag coefficient of the stator to have a significant effect on motor behavior. Because we explicitly model the motion of the stator, we are able to study directly the effect of this parameter on the BFM's torque–speed curve. Our model predicts that increasing the stator drag truncates the torque–speed plateau, thus reducing the concave-down shape of the BFM torque–speed curve (Fig. 6*D*).

This is a direct consequence of the steric forces: Some portion of the stator-generated force must go toward moving the stator itself. As the drag of the stator increases, so does the amount of its generated force allocated to this task. Then, for a given load, the torque transferred to the rotor is relatively low for large stator drag coefficients. This reduces the constant-torque plateau, as well as the overall concave-down shape of the torque–speed curve. This simple prediction may be experimentally tested by increasing the viscosity of the stator's membrane environment. We note that this prediction is not compatible with a linear potential for the rotor–stator interaction (for a detailed discussion, we refer the reader to *SI Text*).

Discussion

The ability to convert a transmembrane ion gradient into rotary torque is rare, observed so far in only two protein motors: the F_O motor of ATP synthase and the BFM. The mechanism behind the torque generation in the latter has been a longstanding mystery, driven by the fundamental role of this machine in bacterial locomotion and chemotaxis.

Here we have combined known structural information on the BFM (5, 15), as well as the experimental measurements on single-stator motors by Lo et al. (3), to construct and test, to our knowledge, the first mechanically specific model of torque generation. Using this information, we are able to present an explicit model of the dynamics of the stator during a torque generation cycle. Our model implicates a steric interaction between the cytoplasmic MotA stator loops and the FliG proteins of the rotor. We have tested the feasibility that this interaction is driven by conformational changes in the MotA loops due to the binding of cations to essential aspartate residues on the two MotBs, as was proposed by Blair and coworkers (5). Results from our model simulations reproduce recently measured torque–speed and speed–IMF curves from single-stator motors. A directly testable prediction of our mechanism is that increasing the stator drag coefficient (e.g., via increasing the membrane viscosity) will reduce the constant-torque plateau, as well as the overall concave-down shape of the torque speed curve.

The mechanism we have proposed is akin to a two-cylinder engine, where two of the four MotA loops act when the motor is moving in the CCW direction and the other two loops act in the CW direction. We have proposed that the two loops act in phase with each other, moving in synchrony as two protons bind to the MotBs and are subsequently released into the cytoplasm. In this manner, the first loop executes its half of the power stroke when the protons bind to the MotBs, and the second loop drives the second half of the power stroke once the protons have hopped off into the cytoplasm.

Experiments performed at low IMF can be used to differentiate between a stator acting as an engine that is in phase or out of phase. Because ion binding is rate limiting under these conditions, trajectories would show clear half-steps only if the BFM acts as an out-of-phase engine. However, given that the mechanics of the power stroke for both scenarios are equivalent, the corresponding out-of-phase mechanism would lead to a calculation analogous to the one presented in this work.

Recently measured torque–speed curves revealed that the number of torque-generating units in the flagellar motor increases with load (2). This opens several fundamental questions regarding the physics of this molecular machine. A fuller treatment of motors with multiple stators requires a model of stator recruitment—a compelling topic for future work.

Finally, viewing our model in a larger context, if it turns out that the proline hinge motif is not the stator structure driving rotation, but another structural motif, then essentially the same equations would have to be solved, albeit using a different set of collective coordinates.

Materials and Methods

The mechanochemistry of the torque generation cycle of a flagellar motor with a single stator unit can be modeled by the following Langevin equations. The dynamics of the angular positions of the stator loops $\phi_S^i(t)$, $i \in \{1,3\}$ are given as

$$\zeta_S \frac{d\phi_S^i}{dt} = \underbrace{-\frac{\partial G}{\partial \phi_S^i}\ell_p}_{\substack{\text{Torque from}\\ \text{Proline hinge}}} - \underbrace{\frac{\partial V_{RS}}{\partial \phi_S^i}}_{\substack{\text{Reaction}\\ \text{from rotor}}} - \underbrace{\frac{\partial \psi}{\partial \phi_S^i}\ell_p}_{\substack{\text{Electrostatic}\\ \text{attraction}}} + \underbrace{\sqrt{2k_BT\zeta_S}f_n(t).}_{\text{Thermal fluctuations}} \quad [1]$$

Here, as in the following equations, the last term is the stochastic Brownian force, where $N(t)$ is uncorrelated white noise; ζ_S is the effective drag coefficient of the stator. $G = G(\phi_S^i, j)$ denotes the free energy of stator loop i, modeled in Fig. 5*B* as a Landau potential. However, because of thermal fluctuations, the exact shape of the potentials is immaterial. Accordingly, we approximate this potential by piecewise quadric functions for ease of computation. The parameter $j \in \{0,2\}$ corresponds to the chemical state of the system: $j = 2$ if two protons are bound to the MotB helices and $j = 0$ if not. The switching between the two chemical states corresponds to a jump between potential curves, as shown in Fig. 5*B*.

As the stator moves between the two configurations, it induces a contact force, and subsequent torque, on the rotor. Unlike previous models, we do not assume that this torque is constant across loads but rather depends on the ζ_L (see *SI Text* for more information). To this end, we do not allow a linear interaction potential between the stator and the FliG; this would result in a constant applied force, which is not true for contact forces. We model the steric interaction potential V_{RS} as

$$V_{RS}(\phi_S^i, \theta_R) = \begin{cases} -F_{RS}\dfrac{(R\theta_R - \ell_P\phi_S^i)^2}{X_{RS}} & \text{if } 0 \le x \le X_{RS} \\ 0 & \text{otherwise,} \end{cases}$$

where $x = X_{RS} + R\theta_R - \ell_P\phi_S^i$ denotes the distance between the position of the stator loop and the nearest FliG. For a graphical depiction, see *SI Text*. From this, the torque imposed on the rotor is calculated as $\tau_{\text{contact}} = -\partial V_{RS}/\partial\theta_R$, whereas the corresponding reaction torque on a stator loop is given by $\tau_{\text{reaction}} = -\partial V_{RS}/\partial\phi_S^i$.

The charges on the FliG and the stator loop exert weak attractive forces on each other. These forces prevent the drifting of the rotor with respect to the stator during the chemical transition events. We refer the reader to *SI Text* for more on the effects of attractive electrostatic forces on the torque–speed curves. With the contact torque and the weak electrostatic forces, the total instantaneous torque on the rotor is given by $\tau = \tau_{\text{contact}} - R(\partial\psi/\partial\theta_R)$. The average torque on the rotor is a time (or ensemble) average of the instantaneous torque. Finally, the rotor and load are connected by a linear

spring with elastic constant κ; the elastic coupling terms in the equations for the rotor and the load thus appear with opposite signs.

Given this, the rotor dynamics are described by a corresponding Langevin equation,

$$\zeta_R \frac{d\theta_R}{dt} = \underbrace{-\frac{\partial V_{RS}}{\partial \theta_R}}_{\text{Torque from stator}} \underbrace{-\frac{\partial \psi}{\partial \theta_R} R}_{\text{Electrostatic attraction}} \underbrace{-\kappa(\theta_R - \theta_L)}_{\text{Connection to load}} + \underbrace{\sqrt{2 k_B T \zeta_R} f_n(t)}_{\text{Thermal fluctuations}}, \quad [2]$$

where ζ_R is the effective rotor drag coefficient. Finally, the dynamics of the load are then driven by the motion of the rotor,

$$\zeta_L \frac{d\theta_L}{dt} = \underbrace{\kappa(\theta_R - \theta_L)}_{\text{Spring connection to rotor}} + \underbrace{\sqrt{2 k_B T \zeta_L} f_n(t)}_{\text{Thermal fluctuations}}. \quad [3]$$

As above, ζ_L is the effective drag coefficient of the load. All parameter values are provided in Table 1.

The above model can be collapsed to explicitly include only the dynamics of a stator with a single loop that generates torque both during its bending (ϕ_S^i increasing) and unbending (ϕ_S^i decreasing). This description is isomorphic to the mechanism described previously (see Fig. 5) because the mechanics of the two halves of the power stroke are equivalent as described above. The equations corresponding to this reduced model are provided in *SI Text*.

As previously (7), we ensure that chemical transitions are localized near potential minima. We choose rate constants for these transitions such that detail balance is maintained. Further details on our modeling of the chemical kinetics, including explicit forms of the rate constants, is provided in *SI Text*.

ACKNOWLEDGMENTS. This manuscript includes an author (K.K.M.) at Lawrence Berkeley National Laboratory under Contract DE-AC02-05CH11231 with the US Department of Energy. The authors acknowledge funding from National Institutes of Health Grant R01-GM110066 (to G.O. and J.A.N.) and a National Science Foundation Integrative Graduate Education and Research Traineeship administered by the Center for Integrative Biomechanics in Education and Research (to J.A.N.). R.M.B. was supported by the Biotechnology and Biological Sciences Research Council and the Engineering and Physical Sciences Research Council.

1. Berg HC (2003) The rotary motor of bacterial flagella. *Annu Rev Biochem* 72:19–54.
2. Lele PP, Hosu BG, Berg HC (2013) Dynamics of mechanosensing in the bacterial flagellar motor. *Proc Natl Acad Sci USA* 110(29):11839–11844.
3. Lo C-J, Sowa Y, Pilizota T, Berry RM (2013) Mechanism and kinetics of a sodium-driven bacterial flagellar motor. *Proc Natl Acad Sci USA* 110(28):E2544–E2551.
4. Braun TF, Al-Mawsawi LQ, Kojima S, Blair DF (2004) Arrangement of core membrane segments in the MotA/MotB proton-channel complex of *Escherichia coli*. *Biochemistry* 43(1):35–45.
5. Kim EA, Price-Carter M, Carlquist WC, Blair DF (2008) Membrane segment organization in the stator complex of the flagellar motor: Implications for proton flow and proton-induced conformational change. *Biochemistry* 47(43):11332–11339.
6. Cordes FS, Bright JN, Sansom MSP (2002) Proline-induced distortions of transmembrane helices. *J Mol Biol* 323(5):951–960.
7. Xing J, Bai F, Berry R, Oster G (2006) Torque-speed relationship of the bacterial flagellar motor. *Proc Natl Acad Sci USA* 103(5):1260–1265.
8. Meacci G, Tu Y (2009) Dynamics of the bacterial flagellar motor with multiple stators. *Proc Natl Acad Sci USA* 106(10):3746–3751.
9. Meacci G, Lan G, Tu Y (2011) Dynamics of the bacterial flagellar motor: The effects of stator compliance, back steps, temperature, and rotational asymmetry. *Biophys J* 100(8):1986–1995.
10. Brown PN, Hill CP, Blair DF (2002) Crystal structure of the middle and C-terminal domains of the flagellar rotor protein FliG. *EMBO J* 21(13):3225–3234.
11. Lowder BJ, Duyvesteyn MD, Blair DF (2005) FliG subunit arrangement in the flagellar rotor probed by targeted cross-linking. *J Bacteriol* 187(16):5640–5647.
12. Happel J, Brenner H (1983) *Low Reynolds Number Hydrodynamics: With Special Applications to Particulate Media* (Springer, New York), Vol 1.
13. Zhou J, Fazzio RT, Blair DF (1995) Membrane topology of the MotA protein of *Escherichia coli*. *J Mol Biol* 251(2):237–242.
14. Zhou J, Lloyd SA, Blair DF (1998) Electrostatic interactions between rotor and stator in the bacterial flagellar motor. *Proc Natl Acad Sci USA* 95(11):6436–6441.
15. Lee LK, Ginsburg MA, Crovace C, Donohoe M, Stock D (2010) Structure of the torque ring of the flagellar motor and the molecular basis for rotational switching. *Nature* 466(7309):996–1000.
16. Sowa Y, et al. (2005) Direct observation of steps in rotation of the bacterial flagellar motor. *Nature* 437(7060):916–919.
17. Nakamura S, Kami-ike N, Yokota JP, Minamino T, Namba K (2010) Evidence for symmetry in the elementary process of bidirectional torque generation by the bacterial flagellar motor. *Proc Natl Acad Sci USA* 107(41):17616–17620.
18. Bai F, Lo C-J, Berry RM, Xing J (2009) Model studies of the dynamics of bacterial flagellar motors. *Biophys J* 96(8):3154–3167.
19. Paul K, Brunstetter D, Titen S, Blair DF (2011) A molecular mechanism of direction switching in the flagellar motor of *Escherichia coli*. *Proc Natl Acad Sci USA* 108(41):17171–17176.
20. Wang H, Oster G (2002) The Stokes efficiency for molecular motors and its applications. *Europhys Lett* 57(1):134.
21. Kojima S, Blair DF (2001) Conformational change in the stator of the bacterial flagellar motor. *Biochemistry* 40(43):13041–13050.
22. Braun TF, et al. (1999) Function of proline residues of MotA in torque generation by the flagellar motor of *Escherichia coli*. *J Bacteriol* 181(11):3542–3551.
23. Berry RM, Berg HC (1997) Absence of a barrier to backwards rotation of the bacterial flagellar motor demonstrated with optical tweezers. *Proc Natl Acad Sci USA* 94(26):14433–14437.
24. Reid SW, et al. (2006) The maximum number of torque-generating units in the flagellar motor of *Escherichia coli* is at least 11. *Proc Natl Acad Sci USA* 103(21):8066–8071.
25. Feng EH, Crooks GE (2008) Length of time's arrow. *Phys Rev Lett* 101(9):090602.
26. Wadhams GH, Armitage JP (2004) Making sense of it all: Bacterial chemotaxis. *Nat Rev Mol Cell Biol* 5(12):1024–1037.
27. Porter SL, Wadhams GH, Armitage JP (2011) Signal processing in complex chemotaxis pathways. *Nat Rev Microbiol* 9(3):153–165.
28. Mora T, Yu H, Sowa Y, Wingreen NS (2009) Steps in the bacterial flagellar motor. *PLOS Comput Biol* 5(10):e1000540.
29. Duke TAJ, Le Novère N, Bray D (2001) Conformational spread in a ring of proteins: A stochastic approach to allostery. *J Mol Biol* 308(3):541–553.
30. Bai F, Minamino T, Wu Z, Namba K, Xing J (2012) Coupling between switching regulation and torque generation in bacterial flagellar motor. *Phys Rev Lett* 108(17):178105.
31. Tipping MJ, Delalez NJ, Lim R, Berry RM, Armitage JP (2013) Load-dependent assembly of the bacterial flagellar motor. *MBio* 4(4):e00551—13.
32. Purcell EM (1977) Life at low Reynolds number. *Am J Phys* 45(1):3–11.
33. Yuan J, Fahrner KA, Turner L, Berg HC (2010) Asymmetry in the clockwise and counterclockwise rotation of the bacterial flagellar motor. *Proc Natl Acad Sci USA* 107(29):12846–12849.
34. Block SM, Blair DF, Berg HC (1989) Compliance of bacterial flagella measured with optical tweezers. *Nature* 338(6215):514–518.
35. Sowa Y, Berry RM (2008) Bacterial flagellar motor. *Q Rev Biophys* 41(2):103–132.
36. Yuan J, Berg HC (2008) Resurrection of the flagellar rotary motor near zero load. *Proc Natl Acad Sci USA* 105(4):1182–1185.